# Defining Reactivity of Solid Sorbents: What Is the Most Appropriate Metric?

Megan Winter,[†] Dambar Hamal,[‡] Xiangxin Yang,[‡] Haidoo Kwen,[†] David Jones,[†] Shyamala Rajagopalan,*[,†] and Kenneth J. Klabunde*[,‡]

*Department of Chemistry, Kansas State University, Manhattan, Kansas 66506, and NanoScale Corporation, 1310 Research Park Drive, Manhattan, Kansas 66502*

*Received December 5, 2008. Revised Manuscript Received April 6, 2009*

A series of solid sorbent materials, including alumina ($Al_2O_3$), magnesia (MgO), titania ($TiO_2$), silica ($SiO_2$), and carbon, of widely varying physical properties, have been studied as sorbents for two toxic substances: sulfur dioxide gas ($SO_2$) and chemical warfare surrogate 2-chloroethyl ethyl sulfide (2-CEES, $ClCH_2CH_2SCH_2CH_3$). Sorbent surface areas, average pore sizes, pore volumes, surface hydroxyl groups, and nitrogen adsorption−desorption isotherms were measured. Surface areas varied from 18 $m^2/g$ to over 1000 $m^2/g$, pore volumes from 0.04 to 1.2 $cm^3/g$, and pore diameters from 1.7 to 4.9 nm. Breakthrough studies of $SO_2$ and 2-CEES sorption yielded information about the effectiveness of each sorbent. Carbon samples worked well for 2-CEES but not $SO_2$, while silica samples were poor for both. The best MgO and $TiO_2$ samples were good for both $SO_2$ and 2-CEES, and overall, the highest surface area (459 $m^2/g$) $TiO_2$ sample was the superior sorbent. The important features for an effective sorbent under the conditions employed are high surface area and high pore volume, possessing isolated surface −OH groups, mesoporous nature, and a polar surface (Lewis base and Lewis acid sites).

## 1. Introduction

Over the past decade, considerable effort has been dedicated to the design and fabrication of nanostructured porous solid materials with functional properties.[1] The composition and exact architecture of the porous structure of solids such as carbons, metal oxides, zeolites, and so forth strongly influence their adsorptive ability for liquids and gases. Despite enormous strides in the synthesis of various classes of nanostructured materials, our understanding of the mechanisms regarding their nucleation and growth and in particular the structural metrics that guide their adsorptive performance is still developing. Understanding the internal porous structure as well as the external surface structure and the relationship of these properties to the performance of the material is a scientifically and technologically important problem, as this will allow the more efficient design of these materials and increase the range of their application. In addition, detailed studies specifically geared toward delineating the comparative performance of compositionally similar but structurally different porous solids are clearly needed to quickly identify key characteristics that one could use in the identification and downselection of promising formulations for a desired end use.

The ability to synthesize new formulations, controlling composition as well as porous structure, is extremely important in materials science. The design of adsorbents with desirable properties will only result from continued improvements in comprehension of structure−function relationships and the utilization of this knowledge in synthesis and application. Generally, development of new sorbents has typically relied on methods that involve empirical studies related to performance testing of formulations of interest. Currently, there is growing interest in using a more systematic scientific approach for sorbent design because achieving the ability to tailor sorbents of choice does have an enormous economic impact.[2] There is no doubt that a clear knowledge of structure−performance correlations will permit development of novel procedures and new formulations based on rational modification of reactants and reaction conditions.

The goal of the current work was to enhance our understanding of structure−performance correlations in various classes of porous sorbents. We chose to examine a series of metal oxides (polar structures) that encompassed low surface area to high surface area with microporous and mesoporous architectures of a random nature (not ordered in pore structure, for example not like MCM-41[2d,e] or SBA-15[2f,g] type materials). Also, we chose to compare a series of carbon based samples, which usually possess comparatively nonpolar surfaces, although several contained additives that would provide some polar surface sites.

The structural characterization study was based on nitrogen adsorption measurements and FT-IR characterization of five magnesium oxides, four titanium dioxides, four aluminum

* Corresponding authors. E-mail: kenjk@ksu.edu (K.J.K.); srajagopalan@nanoscalecorp.com (S.R.).
[†] NanoScale Corporation.
[‡] Kansas State University.

(1) (a) Zhao, X. S.; X., S.; Su, F.; Yan, Q.; Guo, W.; Bao, X. Y.; Lv, L.; Zhou, Z. *J. Mater. Chem.* **2006**, *16*, 637–648. (b) Zhang, H.; Cooper, A. I. *Soft Matter* **2005**, *1*, 107–113. (c) Wakayama, H.; Goto, Y.; Fukushima, Y. *Phys. Chem. Chem. Phys.* **2003**, *5*, 3784–3788. (d) Zub, Y. L.; Seredyuk, I. V.; Chuiko, A. A.; Jaroniec, M.; Jones, M. O.; Parish, R. V.; Mann, S. *Mendeleev Commun.* **2001**, *11*, 208–210. (e) Tanaka, S.; Nishiyama, N.; Egashira, Y.; Ueyama, K. *Chem. Commun.* **2005**, 2125–2127. (f) Guizard, C. G.; Julbe, A. C.; Ayral, A. *J. Mater. Chem.* **1999**, *9*, 55–65.

10.1021/cm8032884 CCC: $40.75 
Published on Web 05/14/2009

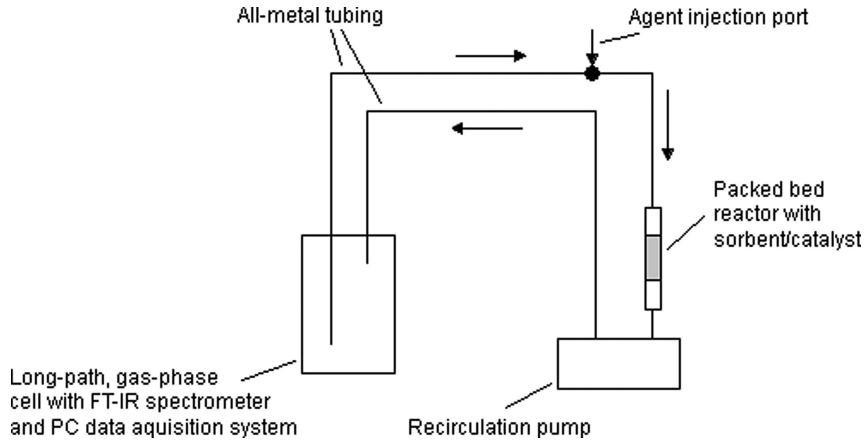


**Figure 1.** Schematic diagram of the testing apparatus.

oxides, three silicas, and six carbon samples. The adsorptive performance of all these sorbents was then evaluated using $SO_2$ (polar and highly toxic industrial chemical) and 2-chloroethyl ethyl sulfide (2-CEES, Mustard agent simulant, hydrophobic) as the adsorbates. Finally, the correlation between the structural data and the adsorptive performance data was assessed for all sorbents to see if indeed there are any generally useful trends that can be identified and applied for new sorbent design.

## 2. Experimental Procedure

**2.1. Chemicals and Sorbents.** Five different classes of sorbents were tested against 2-chloroethyl ethyl sulfide and sulfur dioxide. 2-CEES (98% purity) and $SO_2$ (99.9+% purity) were obtained from Aldrich. Five formulations of MgO (MgO**1**−**5**), four each of $TiO_2$ ($TiO_2$**1**−**4**) and $Al_2O_3$ ($Al_2O_3$**1**−**4**), three formulations of silica ($SiO_2$**1**−**3**), and six carbon formulations (Carbon**1**−**6**) were used in this study. MgO**1**, **2**, and **4** are commercially available samples from NanoScale Corporation and MgO**3** and MgO**5** were purchased from an external commercial supplier. $TiO_2$**1**−**3** are developmental samples from NanoScale and $TiO_2$**4** was purchased from an external commercial supplier and was used as received. $Al_2O_3$**1**−**3** are each available from NanoScale, and $Al_2O_3$**4** is a commercially available sorbent used by the military. All three silica samples ($SiO_2$**1**−**3**) and the six carbon samples (Carbon**1**−**6**) were commercially purchased samples from various suppliers and were used as received.

**2.2. Solid Characterizations.** *2.2.1. Textural Properties of Metal Oxides and Carbon Sorbents.* Nitrogen adsorption−desorption isotherms for all the metal oxide and carbon samples were recorded at 77 K on a NOVA-1200 Instrument from Quantachrome Corporation. The specific surface areas of the sorbents were determined according to the Brunauer−Emmett−Teller (BET) method.[3] The pore size distributions were derived from the desorption branches of corresponding isotherms based on the Barrett−Joyner−Halenda (BJH) method.[4] In addition, pore volumes and pore diameters of all samples were calculated from the BJH desorption isotherms data recorded on the NOVA-1200 Quantachrome Instrument.

**Figure 2.** Long-path gas-phase IR cell, the main component of the testing apparatus.

*2.2.2. DRIFTS-IR.* DRIFT (diffuse reflectance infrared Fourier transform) spectra were recorded on a Nicolet NEXUS 870 infrared spectrometer with a liquid nitrogen cooled MCT detector. The background was collected with KBr (IR grade) purchased from Fluka. All samples except carbons were examined by DRIFT as neat materials. All carbon samples were diluted with anhydrous KBr (sample:KBr = 5:95, w/w) and were ground before analysis. All spectra were recorded at a nominal resolution of 4 $cm^{-1}$.

**2.3. Measurement of Solid Reactivity.** The chemical reactivity of each sorbent was tested using a closed loop flow through test (Figure 1). The experimental setup included a Nicolet 6700 FT-IR (from Thermo Electron Corporation) equipped with a long path cell (model 16-V manufactured by Infrared Analysis, Inc.), a KNF laboratory pump, and a 1 cm diameter glass tube with a coarse glass frit attached inside near the center. Each piece of equipment was connected with metal tubing and the appropriate fittings in a loop (Figure 2).

The internal volume of the cell vessel is 2.5 L. The nitrogen mixed with 2-CEES vapor or $SO_2$ contained in the internal volume of the cell was continuously circulated through a packed bed reactor filled with test material by a diaphragm pump, both presented in Figure 3.

(2) (a) Fernández-García, M.; Martínez-Arias, A.; Hanson, J. C.; Rodriguez, J. A. *Chem. Rev.* **2004**, *104*, 4063–4104. (b) Soler-Illia, G. J. A. A.; Sanchez, C.; Lebeau, B.; Patarin, J. *Chem. Rev.* **2002**, *102*, 4093–4138. (c) Barton, T. J.; Bull, L. M.; Klemperer, W. G.; Loy, D. A.; McEnaney, B.; Misono, M.; Monson, P. A.; Pez, G.; Scherer, G. W.; Vartuli, J. C.; Yaghi, O. M. *Chem. Mater.* **1999**, *11*, 2633–2656. (d) Beck, J. S.; Vartuli, J. C.; Roth, W. J.; Leonowicz, M. E.; Kresge, C. T.; Schmitt, K. D.; Chu, C. T. W.; Olson, D. H.; Sheppard, E. W.; McCullen, S. B.; Higgins, J. B.; Schlenker, J. L. *J. Am. Chem. Soc.* **1992**, *114*, 10834–10843. (e) Kresge, C. T.; Leonowicz, M. E.; Roth, W. J.; Vartuli, J. C.; Beck, J. S. *Nature* **1992**, *359*, 710–12. (f) Zhao, D. Y.; Feng, J. L.; Huo, Q. S.; Melosh, N.; Frederickson, G. H.; Chmelka, B. F.; Stucky, G. D. *Science* **1998**, *279*, 548–552. (g) Zhao, D. Y.; Huo, Q. S.; Feng, J. L.; Chmelka, B. F.; Stucky, G. D. *J. Am. Chem. Soc.* **1998**, *120*, 6024–6036.

(3) Branauer, S.; Emmett, P. H.; Teller, E. *J. Am. Chem. Soc.* **1938**, *60*, 309–319.

**Figure 3.** Packed bed reactor containing sorbent mounted on top of the recirculating pump.

In a representative procedure, the system was purged with nitrogen before testing, granules of the selected sorbent (−35 to +60 mesh) were placed in the glass tube on top of the frit, and the desired reagent was injected through a T-adaptor in the tubing. The pump enabled the continuous flow of the reagent and process nitrogen through the sorbent bed into the FT-IR for analysis and back through the system at a rate of 5.5 LPM. For all flow through tests, 0.1 g of sorbent was used, and agent concentrations in the system were based on a total system volume of 2.5 L. Testing was completed using an 18.9 and 9.35 (w/w) sorbent to agent ratio for $SO_2$ and 2-CEES, respectively. FT-IR scans were taken every minute for a period of 20 min, and specified bands were integrated (1400−1300 $cm^{-1}$ for $SO_2$; 3100−2800 $cm^{-1}$ for 2-CEES). The band areas were converted to the system concentration by application of a calibration equation to obtain an agent concentration profile.

## 3. Results

**3.1. Nitrogen Adsorption Description.** The $N_2$ adsorption−desorption isotherms at 77 K for all oxide (MgO, $TiO_2$, $Al_2O_3$, and $SiO_2$) and carbon sorbents are presented in Figure 4a−e, and their corresponding textural parameters, namely, BET surface areas, pore volumes, and pore diameters, are listed in Table 1.

**3.2. DRIFTS FT-IR.** Next, a broad series of FT-IR studies by the DRIFTS technique was carried out. Spectra for the 22 sorbents were recorded, followed by spectra for each sorbent after being used in $SO_2$ and 2-CEES adsorption experiments, or 66 spectra in all, and with numerous duplicates to check for reproducibility.

Using MgO as an example, Figures 5−7 show pure MgO (all samples) and then used samples exposed to 2-CEES and $SO_2$. These samples (Figure 5) showed absorption bands spanning the 3760−3000 $cm^{-1}$, due to O−H stretching modes of different types, namely, isolated and hydrogen bonded hydroxyl groups; the band at 1640 $cm^{-1}$ was assigned to the molecular water bending mode. For all MgO samples, the band at 1500−1300 $cm^{-1}$ was attributed to carbonate species. In the case of MgO**1** weak bands at around 2900−2700 $cm^{-1}$ and strong absorption around 1200−1000 $cm^{-1}$ were assigned to C−H and C−O stretching, respectively. All samples have strong bands below 1000 $cm^{-1}$, and it is known that oxide samples exhibit strong phonon modes below 1000 $cm^{-1}$.

After adsorption of $SO_2$ (Figure 6), a strong peak appeared at 1020 $cm^{-1}$ due to S═O stretching. Changes were seen in the intensity of the hydroxyl bands as well with all samples.

After adsorption of 2-CEES (Figure 7), several new weak peaks appeared in the region between 3000 and 2860 $cm^{-1}$ for MgO**1**, **2**, **4**, and **5**. These peaks were related to C−H stretching. On the basis of the spectra of neat MgO, MgO/2-CEES, and neat 2-CEES (not shown here), 2-CEES or fragments of 2-CEES were adsorbed on the surface of the MgO samples, except for MgO**3** (a sample that showed little capacity for adsorption; see later discussion). Two other interesting observations are that the isolated OH groups of MgO (except MgO**3**) disappeared after use, and the residual alkoxy groups on MgO**1** were lessened in intensity.

As seen in Figure 8, $TiO_2$ samples showed a very broad absorption in the 3700−2600 $cm^{-1}$, due to the superposition of the O−H stretching mode of interacting hydroxyl groups (those that are involved in hydrogen bonds) and the symmetric and asymmetric O−H stretching modes of molecular water coordinated to $Ti^{4+}$ cations. The band at 3674 $cm^{-1}$ was assigned to O−H stretching of different types of isolated hydroxyl groups; the band at 1626 $cm^{-1}$ was assigned to the molecular water bending mode. For $TiO_2$**2**, the bands at around 1400−1300 $cm^{-1}$ were attributed to carbonate species. All samples have strong bands at 970−930 $cm^{-1}$ (phonon modes).

Comparing the spectra of $TiO_2$ before (Figure 8) and after adsorption of 2-CEES (Figure 9), new bands appeared at 2978 and 2930 $cm^{-1}$, due to C−H stretch. For $TiO_2$**1**, new bands were observed at 1456, 1265, and 1060 $cm^{-1}$. For $TiO_2$**2**, **3**, and **4**, another new band appeared at 1560 $cm^{-1}$. Bands at 1456 and 1560 $cm^{-1}$ were assigned to $CH_3$ rock. And the bands at 1265 $cm^{-1}$ were assigned to SC-$H_2$ scissor. After adsorption of $SO_2$, a small new band appeared at 1126 $cm^{-1}$, possibly due to S═O stretch (Figure 10). Isolated −OH stretch disappeared after use.

As seen in Figure 11, $Al_2O_3$ samples showed a very broad absorption in the 3600−2600 $cm^{-1}$, due to the superposition of the O−H stretching mode of interacting hydroxyl groups (those that are involved in hydrogen bonds) and the symmetric and asymmetric O−H stretching modes of molecular water coordinated to $Al^{3+}$ cations. The band at 3665 $cm^{-1}$ was assigned to O−H stretching of different types of isolated hydroxyl groups; the band at 1640 $cm^{-1}$ was assigned to the molecular water bending mode. The weak band around 1400−1300 $cm^{-1}$ in $Al_2O_3$**3** and **4** was attributed to carbonate species. All samples have strong bands below 1000 $cm^{-1}$.

Comparing the spectra of $Al_2O_3$ before and after adsorption of $SO_2$, no obvious difference was observed, which might be due to the overlap of bands due to carbonate species (1400−1300 $cm^{-1}$) and phonon modes and S═O stretching (asymmetric at 1350 $cm^{-1}$, symmetric at 1020 $cm^{-1}$). After adsorption of 2-CEES, new bands appeared in the region of 3000−2800 $cm^{-1}$, due to C−H stretching. Molecular or fragmented 2-CEES were adsorbed on the surface of $Al_2O_3$.

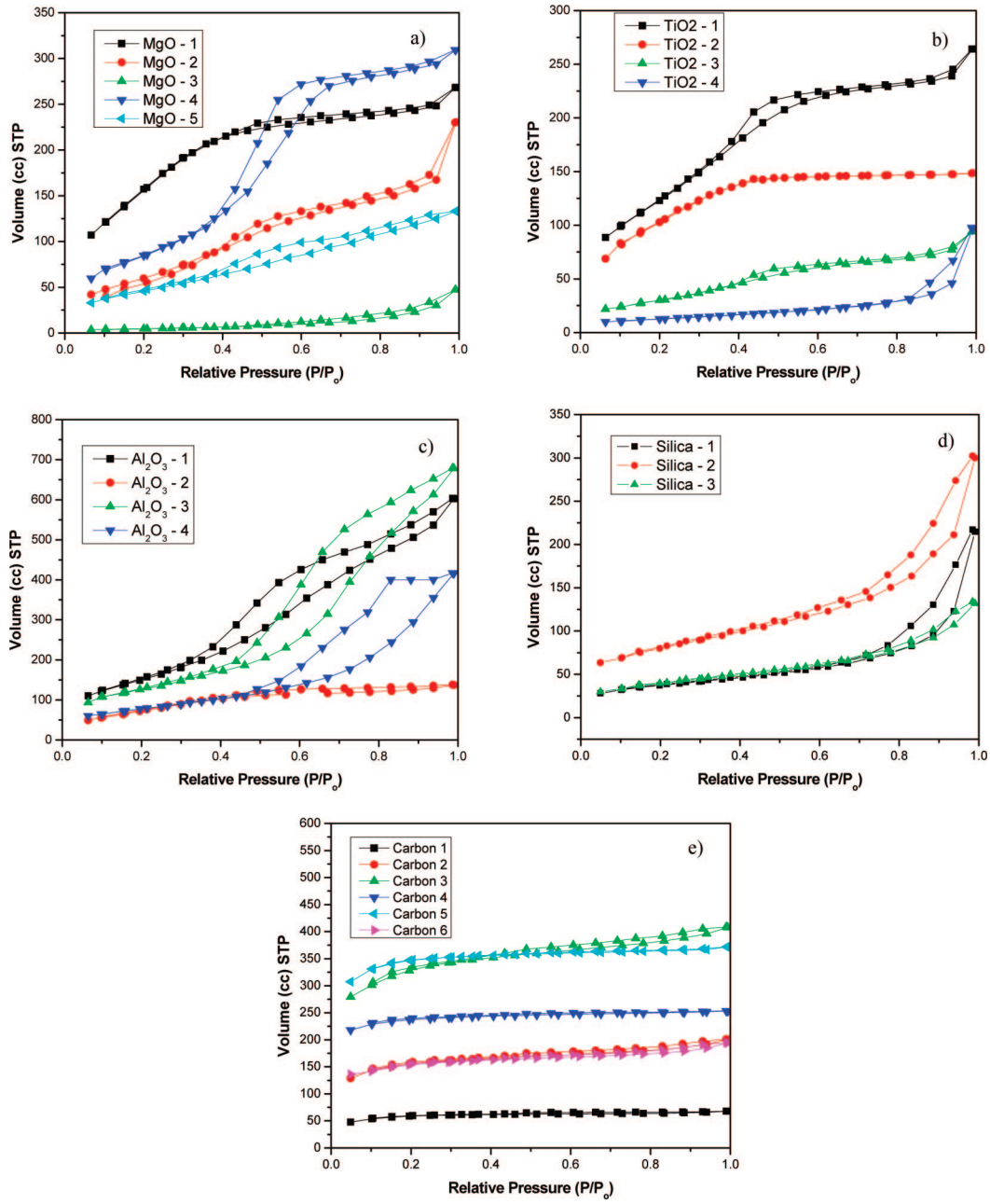


**Figure 4.** $N_2$ adsorption−desorption isotherms for as-received sorbents: (a) MgO, (b) $TiO_2$, (c) $Al_2O_3$, (d) $SiO_2$, and (e) carbon. See Experimental Procedure for sources of samples.

The FT-IR studies of $SiO_2$ and carbon were less helpful. Intense, broad absorption bands for water were observed, as well as several unidentified bands. Upon use for $SO_2$ or 2-CEES adsorption, no real changes could be ascertained for these samples.

**3.3. $SO_2$ and 2-CEES Sorption.** MgO**1** and **4** performed well against both 2-CEES and $SO_2$ as shown in Figures 12 and 13. The agent concentration reduction happened very quickly for both samples within the first 2 min of testing. MgO**3** was ineffective against both 2-CEES and $SO_2$ and MgO**2** and **5** had moderate effectiveness against each agent.

For $TiO_2$ formulations, $TiO_2$**1** had the best performance reducing the overall $SO_2$ concentration to less than 0.1 mL/L and the 2-CEES concentrations to 0.1 $\mu$L/L. The next best performing formulations were $TiO_2$**2** and **3**, respectively. $TiO_2$**4** had poor performance against both $SO_2$ and 2-CEES (Figures 14 and 15).

$Al_2O_3$**1** was the best performing $Al_2O_3$ formulation against both agents but the performance was not as good as the best $TiO_2$ and MgO formulations. The concentration of $SO_2$ was reduced to less than 0.15 mL/L slowly over the length of the test by $Al_2O_3$**1**. The performance against 2-CEES was poor for all alumina formulations (Figures 16 and 17).

The silica samples performed poorly against $SO_2$ with no agent reduction over time (Figures 18 and 19). Silica**2** had the best performance against 2-CEES with a reduction to 0.75 $\mu$L/L.

Carbon**2** performed moderately well against $SO_2$ with a reduction in concentration to 0.15 mL/L. Carbon**3**, **4**, and **6**

**Table 1. Textural Parameters of MgO, $TiO_2$, $Al_2O_3$, $SiO_2$, and Carbon Sorbents**

| sorbent | BET surface area ($m^2/g$) | pore volume ($cm^3/g$) | pore diameter (nm) |
|---|---|---|---|
| MgO**1** | 593 | 0.42 | 2.0 |
| MgO**2** | 227 | 0.40 | 3.3 |
| MgO**3** | 18 | 0.08 | 3.7 |
| MgO**4** | 326 | 0.56 | 3.7 |
| MgO**5** | 341 | 0.09 | 3.7 |
| $TiO_2$**1** | 459 | 0.42 | 3.3 |
| $TiO_2$**2** | 380 | 0.21 | 2.0 |
| $TiO_2$**3** | 113 | 0.16 | 3.3 |
| $TiO_2$**4** | 45 | 0.15 | 2.6 |
| $Al_2O_3$**1** | 557 | 1.0 | 3.3 |
| $Al_2O_3$**2** | 276 | 0.22 | 2.6 |
| $Al_2O_3$**3** | 453 | 1.2 | 4.9 |
| $Al_2O_3$**4** | 275 | 0.68 | 4.9 |
| $SiO_2$**1** | 129 | 0.32 | 1.7 |
| $SiO_2$**2** | 276 | 0.44 | 1.7 |
| $SiO_2$**3** | 138 | 0.20 | 1.7 |
| Carbon**1** | 192 | 0.04 | 1.7 |
| Carbon**2** | 509 | 0.14 | 1.7 |
| Carbon**3** | 1080 | 0.27 | 1.7 |
| Carbon**4** | 759 | 0.07 | 1.7 |
| Carbon**5** | 1100 | 0.12 | 1.7 |
| Carbon**6** | 497 | 0.13 | 1.7 |

also had moderate performance against $SO_2$. All carbon formulations performed well against 2-CEES with nearly 100% reduction in concentration (Figures 20 and 21).

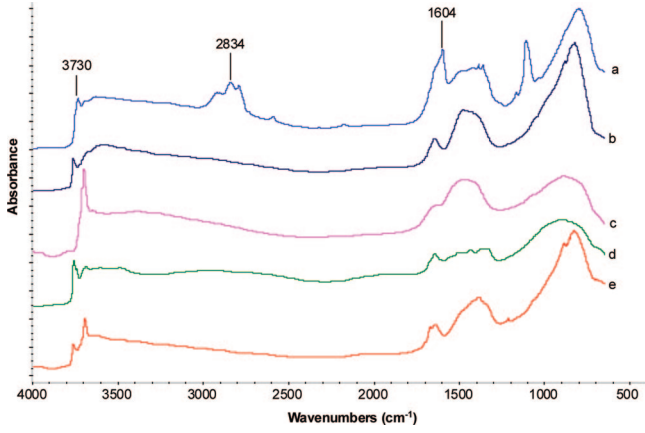


**Figure 5.** IR Spectra of Different MgO: (a) MgO**1**, (b) MgO**2**, (c) MgO**3**, (d) MgO**4**, and (e) MgO**5**.

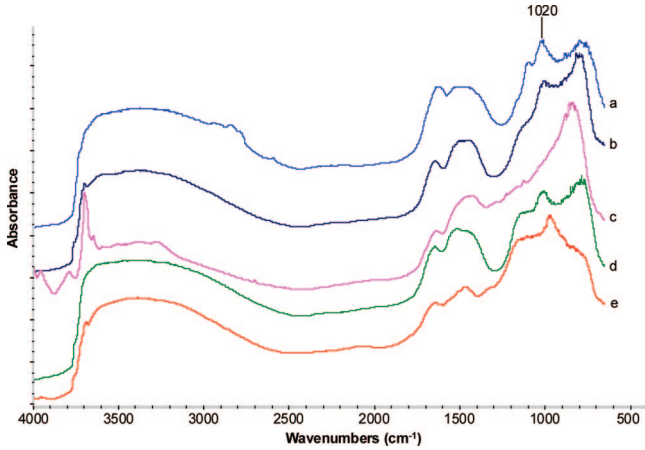


**Figure 6.** IR Spectra of MgO after $SO_2$ adsorption: (a) MgO**1**, (b) MgO**2**, (c) MgO**3**, (d) MgO**4**, and (e) MgO**5**.

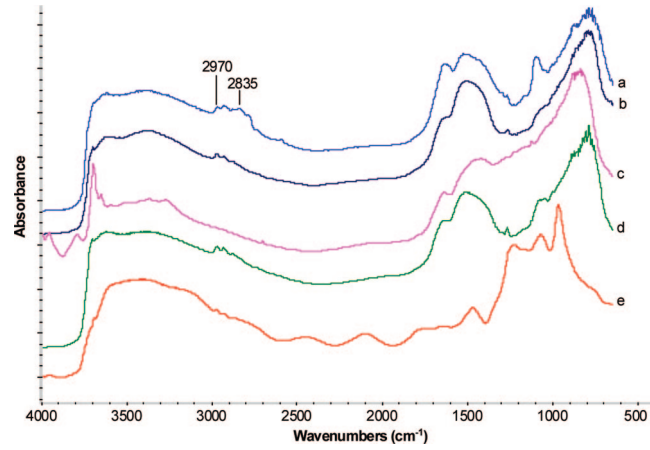


**Figure 7.** IR Spectra of MgO after 2-CEES adsorption: (a) MgO**1**, (b) MgO**2**, (c) MgO3, (d) MgO**4**, and (e) MgO**5**.

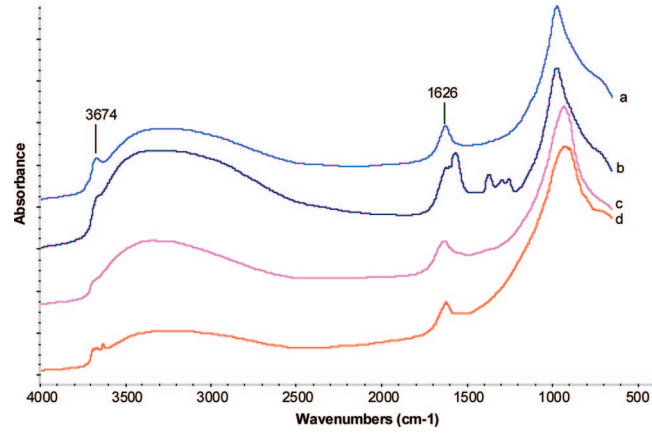


**Figure 8.** IR Spectra of Different $TiO_2$: (a) $TiO_2$**1**, (b) $TiO_2$**2**, (c) $TiO_2$**3**, and (d) $TiO_2$**4**.

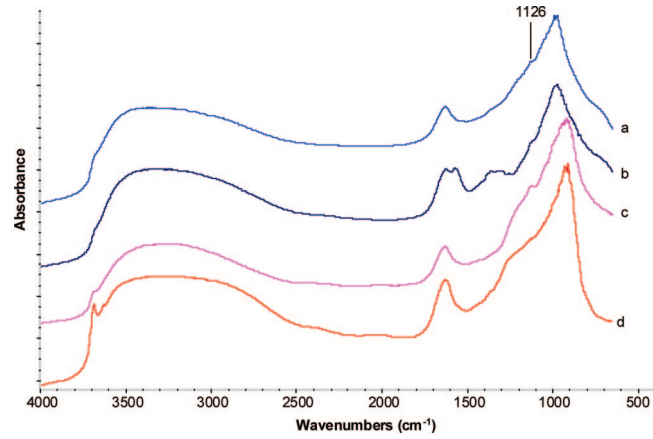


**Figure 9.** IR Spectra of $TiO_2$ after 2-CEES adsorption: (a) $TiO_2$**1**, (b) $TiO_2$**2**, (c) $TiO_2$**3**, and (d) $TiO_2$**4**.

## 4. Discussion

**4.1. MgO.** Five different magnesium oxide samples were evaluated. These materials varied widely in physical characteristics as well as in adsorption performance against the target agents. One MgO material (MgO**3**) performed poorly against both agents with no adsorption of 2-CEES and negligible adsorption of $SO_2$. It had the lowest specific surface area (18 $m^2/g$) and an extremely low pore volume (0.08 $cm^3/g$). The best performers remove 80% or more of

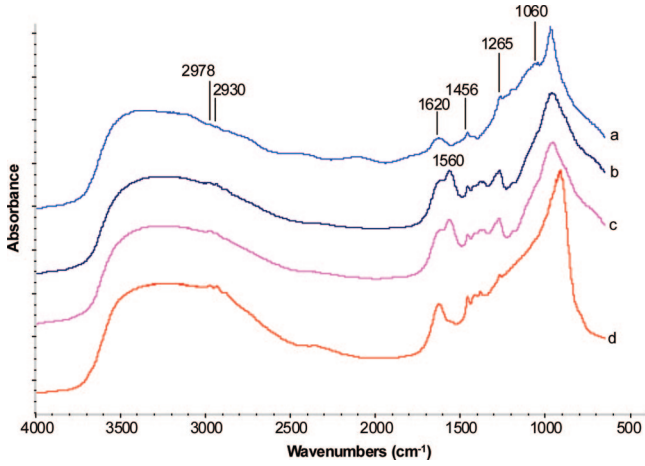


**Figure 10.** IR Spectra of $TiO_2$ after $SO_2$ adsorption: (a) $TiO_2$**1**, (b) $TiO_2$**2**, (c) $TiO_2$**3**, and (d) $TiO_2$**4**.

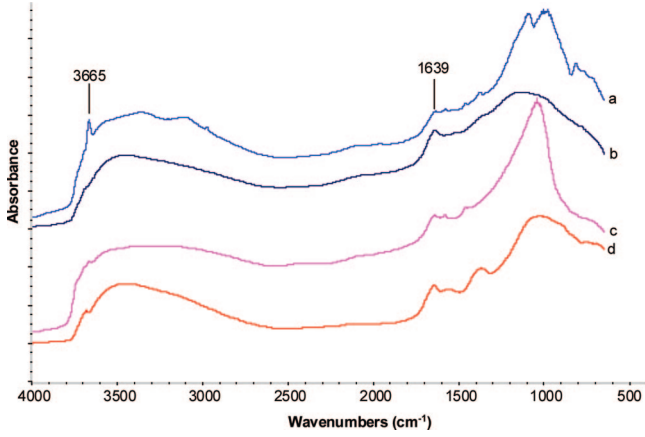


**Figure 11.** IR Spectra of Different $Al_2O_3$: (a) $Al_2O_3$**1**, (b) $Al_2O_3$**2**, (c) $Al_2O$**3**, and (d) $Al_2O_3$**4**.

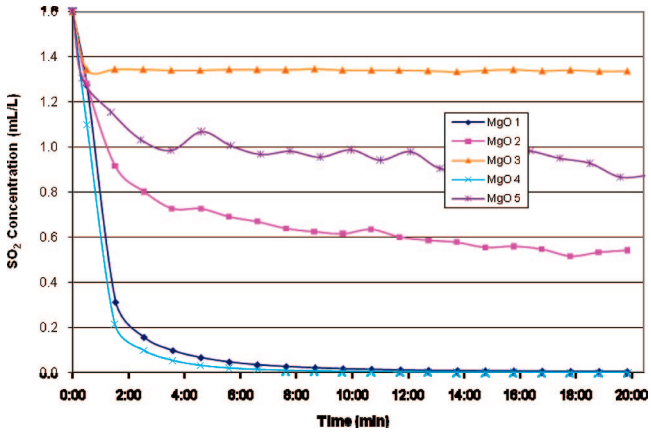


**Figure 12.** Flow testing results for MgO formulations against $SO_2$. The flow tests were carried out in duplicate with observed variation in <3% range.

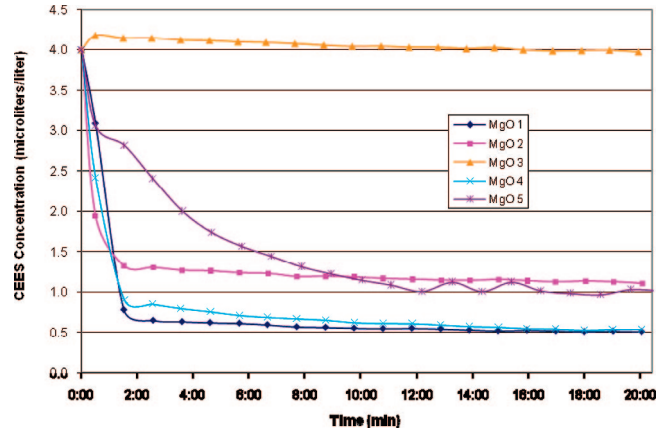


**Figure 13.** Flow testing results for MgO formulations against 2-CEES. The flow tests were carried out in duplicate with observed variation in <3% range.

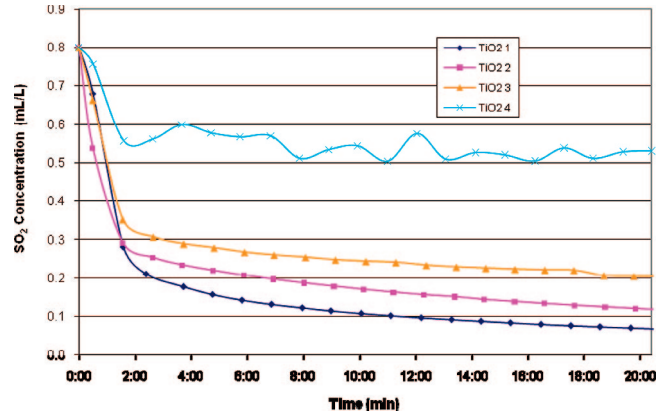


**Figure 14.** Flow testing results for $TiO_2$ formulations against $SO_2$. The flow tests were carried out in duplicate with observed variation in <3% range.

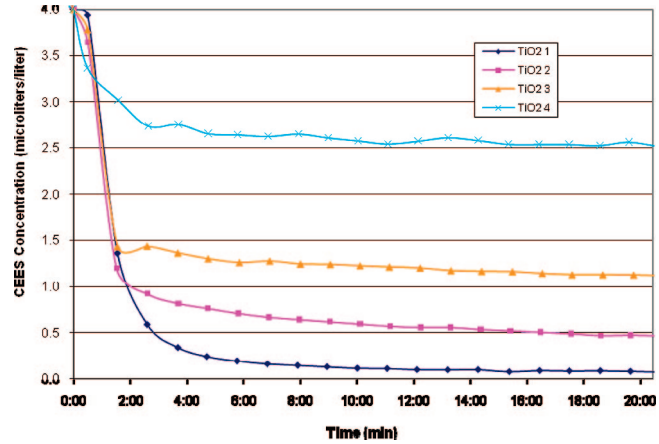


**Figure 15.** Flow testing results for $TiO_2$ formulations against 2-CEES. The flow tests were carried out in duplicate with observed variation in <3% range.

the test agent (MgO**1** and **4**) and had some characteristics in common such as high specific surface area and large pore volumes (593 $m^2/g$, 0.42 $cm^3/g$ and 326 $m^2/g$, 0.56 $cm^3/g$, respectively). MgO**2** and **5** performed better than the worst removing 30−75% of the challenge agent, but not nearly as well as the best. They also had relatively high surface areas, and MgO**2** had a pore volume comparable to the best performers but had no trace organics detectable by IR. This combination of high surface area and large pore volume and coupled with low levels of surface impurities provides the best adsorption performance for MgO against the agents used in this study.

**4.2. $TiO_2$.** Four different titanium dioxide materials were tested in this study. The specific surface area of the materials ranged over an order of magnitude from 45 to about 450 $m^2/g$. The pore volumes were all about 0.2 $cm^3/g$ except for

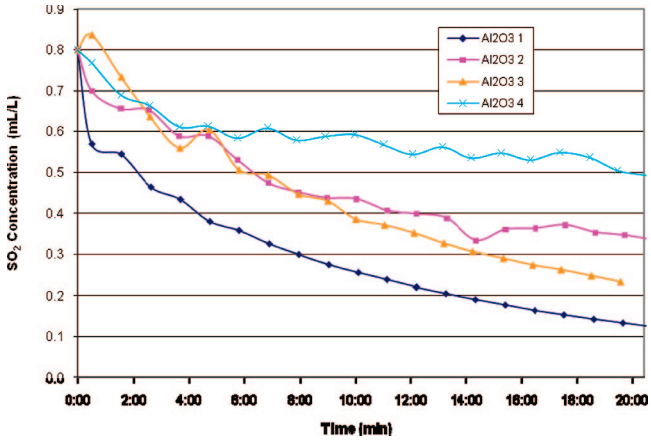


**Figure 16.** Flow testing results for $Al_2O_3$ formulations against $SO_2$. The flow tests were carried out in duplicate with observed variation in <3% range.

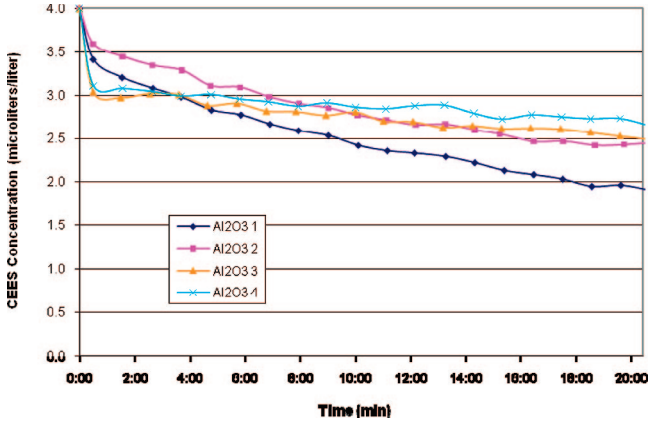


**Figure 17.** Flow testing results for $Al_2O_3$ formulations against 2-CEES. The flow tests were carried out in duplicate with observed variation in <3% range.

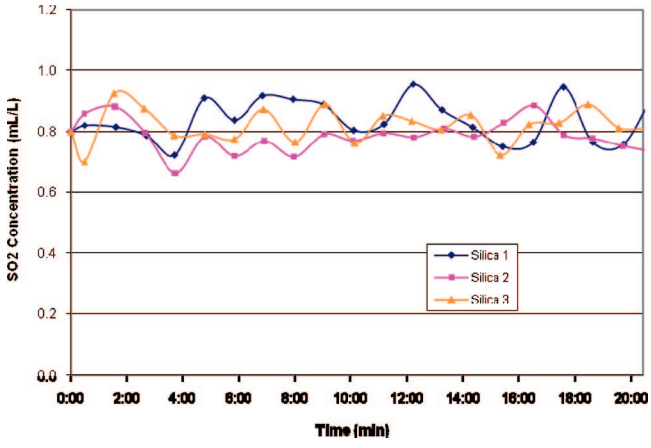


**Figure 18.** Flow testing results for silica formulations against $SO_2$. The flow tests were carried out in duplicate with observed variation in <3% range.

$TiO_2$**1** which had the highest surface area at about 450 $m^2/g$ and twice the pore volume at 0.42 $cm^3/g$. $TiO_2$**4**, which had the lowest specific surface area at 45 $m^2/g$ and a pore volume of 0.15 $cm^3/g$, performed poorly against both agents used. The rest of the titanium dioxide materials performed significantly better with $TiO_2$**1** performing the best. The performance of these materials against the target agents correlated generally with the specific surface area. The

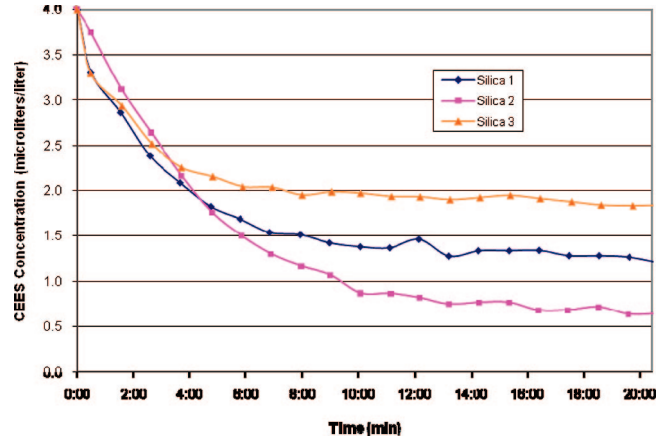


**Figure 19.** Flow testing results for silica formulations against 2-CEES. The flow tests were carried out in duplicate with observed variation in <3% range.

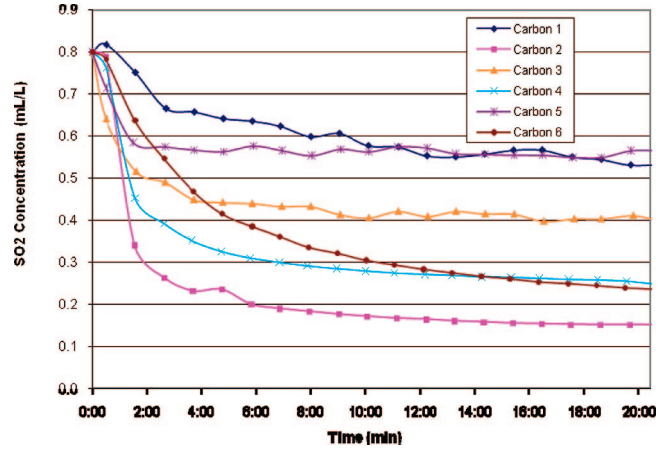


**Figure 20.** Flow testing results for carbon formulations against $SO_2$. The flow tests were carried out in duplicate with observed variation in <3% range.

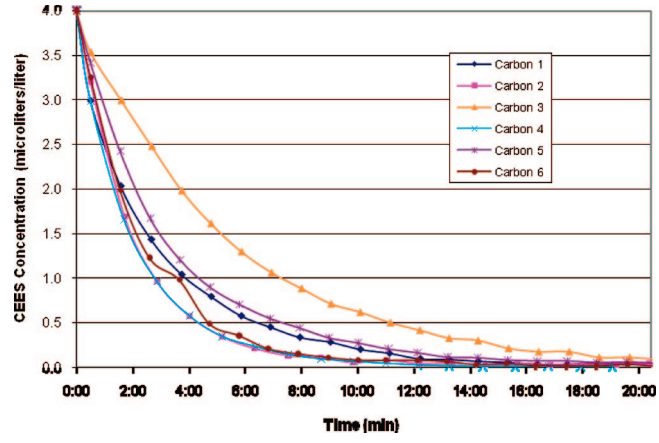


**Figure 21.** Flow testing results for carbon formulations against 2-CEES. The flow tests were carried out in duplicate with observed variation in <3% range.

combination of high surface area and large pore volume provided the best performance.

**4.3. $Al_2O_3$.** Four alumina materials were evaluated. The specific surface areas of these materials ranged from 275 $m^2/g$ to 560 $m^2/g$ and pore volumes from 0.2 to 1.2 $cm^3/g$. The material with the highest specific surface area ($Al_2O_3$**1**) performed the best against the test agents. However, large

surface areas and pore volumes did not necessarily correlate to sorption performance. $Al_2O_3$**2** and **3** performed equally well against both the polar and the nonpolar agents despite the differences in textural properties. $Al_2O_3$**2** and **3** had specific surface areas and pore volumes of 275 and 453 $m^2/g$ and 0.2 and 1.2 $cm^3/g$, respectively. $Al_2O_3$**3** also had increased surface entities in the form of free hydroxyls.

**4.4. $SiO_2$ and Carbon.** Three commercially purchased silicas were tested. None of the samples tested adsorbed any $SO_2$. Performance against 2-CEES was better and distinguished the three silica materials from each other, although there was no correlation to specific surface area or pore volume. Similar to silica, all of the carbons performed well against the nonpolar agent and poorly against the $SO_2$. Performance did not correlate to the textural properties.

**4.5. Conclusions.** On the basis of the physical and chemical characteristics versus performance data acquired during the course of this research, there is no single characteristic that defines adsorptive performance against the agents used. Chemical properties of the substrate seem to play a primarily important role. The amount and type of minor surface moieties also seems to be significant in some cases. It appears that the textural properties are important to a point but play a secondary role to the chemistry. As long as the sorbent provides the proper pore structure and pore volume to meet minimum requirements, the chemical properties define the adsorptive capacity and kinetics of solid sorbents.

Naturally, this variation in textural parameters resulted from the different types and methods of processing final materials. Furthermore, the results of the $N_2$ adsorption−desorption isotherms shown in Figure 4a−e and Table 1 indicated that almost all MgO, $TiO_2$, and $Al_2O_3$ samples have mesoporous structures, whereas all $SiO_2$ and Carbon samples have microporous structures. Moreover, the nature of the observed isotherms and appearance of hysteresis loops reflect the extent of pore uniformity and pore connectivity.[1] For example, sample MgO**4** possesses a type IV isotherm with a characteristic H1 hysteresis loop ($P/P_0 = 0.4-0.7$), clearly indicating its relatively cylindrical pore size uniformity and facile pore connectivity compared to other MgO samples. Similar behavior was observed with the sample $TiO_2$**1** at the relative pressure range ($P/P_0 = 0.4-0.7$) due to the capillary condensation and evaporation in the mesopores. On the other hand, sorbents $Al_2O_3$**1**, **3** and **4** and $SiO_2$**1** and **2** possess type IV isotherms with a H3 hysteresis loop, representing materials comprised of aggregates (loose assemblages) of platelike particles forming slitlike pores. However, Carbon**1**−**6**, MgO**3** and **5**, $TiO_2$**2**, **3**, and **4**, $Al_2O_3$**2**, and $SiO_2$**3** sorbents display type I isotherm monolayer adsorption without any hysteresis loops. Therefore, on the basis of the $N_2$ adsorption−desorption studies, all aforementioned sorbents possess a wide range of the BET surface areas, pore volumes, pore diameters, and pore shapes which could affect their sorption properties.

The $SO_2$ and 2-CEES data show that carbon sorbents worked well for relatively nonvolatile and nonpolar 2-CEES but poorly for volatile, polar $SO_2$, while silica was poor for both. The MgO and $TiO_2$ were superior to $Al_2O_3$ for $SO_2$ and 2-CEES, where MgO was best for $SO_2$ and $TiO_2$ was best for 2-CEES. (An added important benefit is the fact that "destructive adsorption" occurs on the oxides,[5] and therefore, more detoxification of the challenge agents occurs on the oxide surfaces than on carbon.)

The best $TiO_2$ samples were better than carbon and better than MgO or $Al_2O_3$ for $SO_2$ and for 2-CEES. These data indicate that high surface area $TiO_2$ was the most effective pure material as a sorbent under the conditions employed. The key to the behavior of the best $TiO_2$ sample ($TiO_2$**1**) can be explained by the following observations: (1) high surface area; (2) high pore volume; (3) possession of isolated surface-OH groups that are consumed upon use; (4) mesoporous nature with good pore connectivity; and (5) polar surface (Lewis base and Lewis acid sites).

**Acknowledgment.** The financial support of the Army Research Office through their STTR program (Contract No. W911SR-06-C-0054) is acknowledged with gratitude.

CM8032884

(4) Barrett, E. P.; Joyner, L. G.; Halenda, P. P. *J. Am. Chem. Soc.* **1951**, *73*, 373–380.

(5) (a) Rajagopalan, S.; Koper, O.; Decker, S.; Klabunde, K. J. *Chem.—Eur. J.* **2002**, *8*, 2602–2607. (b) Klabunde, K. J., Ed. *Nanoscale Materials in Chemistry*; Wiley Interscience: New York, 2001. Also, two chapters written for this book: (c) Klabunde, K. J. Introduction to Nanotechnology, Chapter 1, pp 1−13. (d) Klabunde, K. J.; Mulukutla, R. Chemical and Catalytic Aspects of Nanocrystals, Chapter 7, pp 223−261. (e) Wagner, G. W.; Koper, O. B.; Lucas, E.; Decker, S.; Klabunde, K. J. *J. Phys. Chem. B* **2000**, *104*, 5118–5123. (f) Wagner, G. W.; Bartram, P. W.; Koper, O.; Klabunde, K. J. *J. Phys. Chem. B* **1999**, *103*, 3225–3228. (g) Klabunde, K. J.; Stark, J. V.; Koper, O.; Mohs, C.; Park, D. G.; Decker, S.; Jiang, Y.; Lagadic, I.; Zhang, D. *J. Phys. Chem.* **1996**, *100*, 12142–12153 (invited Feature Article). (h) Koper, O. B.; Lagadic, I.; Volodin, A.; Klabunde, K. J. *Chem. Mater.* **1997**, *9*, 2468–2480. (i) Klabunde, K. J. Nanometer Sized Metal Oxide Particles for Ambient Temperature Adsorption of Toxic Chemicals. U.S. Patent 5,990,373, November 23, 1999. (j) Koper, O; Klabunde, K. J. Nanoparticles for the Destructive Sorption of Biological and Chemical Contaminants. U.S. Patent 6,057,488; May 2, 2000.